WILEY-VCH

High-Efficiency Anion Exchange Membrane Water Electrolysis Employing Non-Noble Metal Catalysts

*Pengzuo Chen and Xile Hu**

Laboratory of Inorganic Synthesis and Catalysis, Institute of Chemical Sciences and Engineering, Ecole Polytechnique Fédérale de Lausanne (EPFL), CH-1015 Lausanne, Switzerland

E-mail: xile.hu@epfl.ch Website: lsci.epfl.ch

Keywords: Water splitting • Electrocatalysis • Electrolyser • Anion-exchange membrane • NiMo

Abstract:

Alkaline anion exchange membrane (AEM) water electrolysis is a promising technology to produce hydrogen using renewable energies. However, current AEM electrolysers still employ noble-metal-containing electrocatalysts, or have significant overpotential loss, or both. Here we develop non-noble-metal electrocatalysts for both the hydrogen and oxygen evolution reactions (HER and OER). Both catalysts are made of a same NiMo oxide. Judicious processing of this materials in a mixed NH_3/H_2 atmosphere resulted in a NiMo-NH_3/H_2 catalyst, which had superior activity in HER, delivering 500 mA cm^{-2} at an overpotential of 107 mV. Doping Fe ions into the NiMo-NH_3/H_2 catalyst yielded an Fe-NiMo-NH_3/H_2 catalyst, which was highly active for OER, delivering 500 mA cm^{-2} at an overpotential of 244 mV. These catalysts were integrated into an AEM electrolyser, which delivered 1.0 A cm^{-2} at 1.57 V at 80 °C in 1 M KOH. The energy conversion efficiency at this current density is as high as 75%. Our work demonstates high-efficiency AEM electrolysis using earth-abundant catalytic materials.

Low-temperature electrochemical water splitting offers a way of converting electrical power generated from renewable energy into clean hydrogen fuel.[1] Three types of electrolysers have been developed, including alkaline liquid electrolyte (AE), proton exchange membrane (PEM), and anion exchange membrane (AEM) electrolysers.[2–7] The AEM electrolyser combines the advantages of both AE and PEM electrolysers, as it can employ non-noble-metal electrocatalysts as in AE electrolyser, and has a membrane separator as in PEM electrolyser. However, the AEM electrolyser is still at its early stage of development, and there is still large room of improvement in device efficiency, especially when non-noble-metal catalysts are employed.[8–10] In a recent report, an advanced AEM electrolyser with non-noble-metal catalysts had a cell voltages of 1.9 V for 1 A cm^{-2} in 1 M KOH at 60 °C.[11] A record-low cell voltage of 1.59 V was obtained at 1.0 A cm^{-2} at 80 °C, but using a noble-metal catalyst for HER, and a non-noble-metal catalyst (NiFe LDH) for OER.[12] Here we report an AEM electrolyser that operates at 1.57 V for 1.0 A cm^{-2} at 80 °C, the lowest for any AEM electrolyser. Our electrocatalysts are based on the same base material, NiMo oxide. We develop simple and straight-forward activation methods of this non-noble-metal oxide that leads to superior HER and OER catalysts.

NiMo is known as an active HER catalyst in alkaline medium;[13–16] however, it has rarely been applied in AEM electrolyer. We first sought to deposit high-surface-area NiMo catalyst layer on a conductive support. Our approach involved the reduction of an oxide, $NiMoO_4$, to NiMo particles embed in nanowires by annealing the former in a reductive atmosphere at a high temperature. After a few trials, we found that HER-active NiMo compounds could indeed be produced by annealing $NiMoO_4$ on nickel form (NF) in pure NH_3, H_2/NH_3 (5% H_2) or H_2/N_2 (5% H_2) for 2 h at 450 °C to 600 °C. The HER activity of these samples was first screened by linear sweep voltammetry (LSV) in 1 M KOH at a scan rate of 1 mV s^{-1}. The annealing temperature influenced strongly the HER activity of samples, with a similar trend observed for catalysts annealed in different gas atmospheres (Fig. ~~S6~~S1). The optimal temperature was 550

°C (Fig. 1a). Transimission electronc microscopy (TEM) images show subtle differences of morphology for samples synthesized at different temperatures (Fig. S2-4). According to X-ray powder diffraction (XRD) patterns, the $NiMoO_4$ precursor was completely transformed to NiMo at 500 °C or a higher temperature (Fig. S5). The electrochemical surface areas (ECSA) of the samples were estmiated by their electrochemical double-layer capacitances (Fig. S6). The samples synthesized at 550 °C have the highest ECSAs. Thus, annealing at 550 °C gave samples with the highest surface area and appropriate morphology, leading to optimized HER activity.

Among the optimized catalysts, the geometric activity had the order of NiMo-NH_3/H_2 > NiMo-N_2/H_2 ≈ NiMo-NH_3 (Fig. 1b). All three annealed catalysts were much more active than the $NiMoO_4$ precursor and the NF support. The NiMo-NH_3/H_2 catalyst required only 11 mV and 107 mV for a current density of 10 mA cm^{-2} and 500 mA cm^{-2}, respectively. This catalyst had also the lowest Tafel slope of 35 mV dec^{-1} among all catalysts (Fig. 1c). The HER actvity determined by electrochemical impedance spectroscopy (EIS) agreeed with that determined by LSV, with NiMo-NH_3/H_2 having the the smallest charge transfer resistance (Fig. S7). The apparent catalytic stability of NiMo-NH_3/H_2 catalyst was confirmed in a 20 h electrolysis at -0.1 V, where the current density showed negligible change (Fig. S8).

The ECSA of the four optimized NiMo-based HER catalysts were comapared (Fig. S9, S10 and Table S1). Reductive annealing of $NiMoO_4$ led to particles with up to 2.5 times higher ECSA. NiMo-NH_3/H_2 and NiMo-N_2/H_2 have similar ECSAs, which are about 25% higher than that of NiMo-NH_3. This result suggests annealing under an H_2 atmosphere increases the surface area. The ECSA-normalized LSV curves (Fig. 1d) indicate the specific activity of the catalysts. The activity follows the order of NiMo-NH_3/H_2 > NiMo-N_2/H_2 ≈ NiMo-NH_3 at $\eta < 150$ mV. At higher overpotentials, NiMo-NH_3 is more active than NiMo-N_2/H_2 due to a lower Tafel slope.

X-ray photoelectron spectroscopy (XPS) was employed to analyse the compositions and valence states of metals in the optimized NiMo-NH_3/H_2, NiMo-N_2/H_2 and NiMo-NH_3 samples (Fig. S11). Both All samples Ni^0 and Ni^{2+} as well as Mo^0, Mo^{4+} and Mo^{6+}. The ratio of Ni^0/Ni^{2+} decreases from 0.25 to 0.22 and to 0.18 going from NiMo-N_2/H_2 to NiMo-NH_3/H_2 and to NiMo-NH_3. Likewise, the ratio of Mo^0/Mo^{4+} decreases from 0.52 to 0.43 and to 0.40 in this series (Table S2). Assuming Ni^0 and Mo^0 originate from the reduced NiMo alloy, these data indicate that H_2 gas is more efficient than NH_3 in reducing the $NiMoO_4$ precursor. XPS also indicated the presence of N in NiMo-NH_3/H_2 and NiMo-NH_3. The XRD patterns of NiMo catalysts indicates the main phase of NiMo alloy by using H_2/N_2 gas, but the appearance of $NiMoN_x$ phase after adding NH_3 gas (Fig. S12). Previous work showed that the incorporation of N atom into the framework of NiMo, as in $NiMoN_x$, increased the HER activity.[17] The superior activity of NiMo-NH_3/H_2 in this series of catalysts, therefore, might be attributed to having both a $NoMoN_x$ component as well as a high proportion of NiMo.

For OER in alkaline medium, NiFe oxyhydroxide has proven to be the benchmark catalyst.[18–22] We previously reported a non-conventional NiFe catalyst composed of FeOOH nanoclusters anchored on a NiOOH support.[23] An NF electrode loaded with this catalyst could deliver 100 mA/cm^2 at an overpotential of 248 mV in 1 M KOH at 20 ^oC. The catalyst was prepared by electrochemical oxidation of a Ni support to form NiOOH in the presence of residual Fe ions. We wondered whether the NiMo HER catalysts developed above could be converted into NiMoFe oxyhydroxides following a similar method, and whether such oxyhydroxides could deliver even higher geometric activity. There were precedents where a trimetallic CoFeW oxide exhibited higher activity than related bimetallic catalysts.[24,25]

Accordingly, we subjected NiMo-NH_3/H_2, NiMo-N_2/H_2 and NiMo-NH_3, as well as reference compounds $NiMoO_4$ and NF, to anodic oxidation from 1.3 to 1.5 V vs RHE in 1 M KOH in the

presence of iron ions. The resulting samples were denoted as Fe-NiMo-NH_3/H_2, Fe-NiMo-N_2/H_2, Fe-NiMo-NH_3, Fe-$NiMoO_4$ and Fe-NF, respectively. TEM images showed the surfaces of Fe-NiMo-based catalysts became amorphous after oxidation (Fig. S13). XPS spectra indicated the incorporation of Fe ions. Inductively coupled plasma optical emission spectrometry (ICP-OES) analysis revealed the loading of FeOOH as 140 to 160 ug cm^{-2} (Table 1).

The OER activity of the above samples was first screened by LSV in 1 M KOH at 20 ºC. All polarization curves were IR-corrected and the backward scan curves were collected to avoid the influence of Ni oxdiation peak (Fig. S14). As expected, the incorporation of Fe resulted in significant improvement of activity compared to Fe-free samples (Fig. S15). The samples derived from chemically reduced NiMo species were more active than that derived from $NiMoO_4$, which was in turn more active than NF alone (Fig. 2a). Like in the case for HER, annealing at 550 ºC resulted in the highest activity for all three Fe-NiMo-based catalysts (Fig. S16). Interestingly, the catalyst derived from Fe-NiMo-NH_3/H_2, the best HER catalyst, gave the highest geometric OER activity. The overpotentials of this catalyst are 192 mV, 219 mV, and 244 mV for a current density of 10, 100, and 500 mA cm^{-2} respectively (Fig. 2a). These numbers represent an improvement of about 30 mV compared to the analogus FeNi catalyst (table S5 and Fig. 2d). The electrochemical surface areas (ECSA) of the four Fe-NiMo-based OER catalysts were estimated from their electrochemical double-layer capacitances (C_{dl}) (Fig. S17 and S18). The ECSA-normalized LSV curves are shown in Fig. 2c. The Fe-NiMo-NH_3/H_2 and Fe-NiMo-NH_3 catalysts have similar specific activity, followed by Fe-NiMo-H_2 and then Fe-$NiMoO_4$. The activity of these catalysts might be further compared by their turnover frequencies, using the number of maximum Fe-Ni units as the active site (Fig. S19). The TOFs follow the order of Fe-NiMo-NH_3/H_2 > Fe-NiMo-NH_3 > Fe-NiMo-N_2/H_2 > Fe-$NiMoO_4$ > Fe-NF (Table 1). Similar values of TOFs were obtained on samples loaded on carbon cloth (Fig.

S20). The TOF of Fe-NiMo-NH_3/H_2 at n = 220 mV is about 10 times higher than the previously reported and analogous Fe-Ni catalyst (Fig 2b).[23] The four catalysts Fe-NiMo-NH_3/H_2, Fe-NiMo-N_2/H_2, Fe-NiMo-NH_3, Fe-$NiMoO_4$ all have Tafel slopes close to 30 mV dec^{-1} (Fig. S21a). The trend of OER activity, determined by EIS analysis (Fig. S21b and Table 1), agrees with the results from the LSV. The Fe-NiMo-NH_3/H_2 catalyst retained its OER activity after 1000 CV cycles (Fig. S22). Moreover, the apparent catalytic stability of Fe-NiMo-NH_3/H_2 in OER was confirmed in a 18 h electrolysis at 1.46 V (Fig. S23), where the current density remained at about 220 mA cm^{-2}.

All three catalysts (Fe-NiMo-NH_3/H_2, Fe-NiMo-N_2/H_2, Fe-NiMo-NH_3) were detached from the NF electrodes after anodic activation and the samples were subjected to TEM analysis. The Fe-NiMo catalysts became amorphous after oxidation (Fig. 3a, b and Fig. S13). Energy dispersive spectroscopy (EDS) mapping revealed uniform elemental distributions of Ni, Fe, N, O and Mo (Fig. 3d and Fig. S24, S25). However, comparing to the samples before anodic activation, the signals of Mo and N elements in Fe-NiMo catalysts were very weak after anodic activation (Fig. 3c and Table S3). Taking Fe-NiMo-NH_3/H_2 as an example, the contents of Mo and N were about 15.1% and 10.5% in NiMo-NH_3/H_2, but after anodic activation, these contents decreased to only 1.4% and 1.8%, respectively. ICP-OES measurements confirmed the loss of Mo and N after anodic activation. The XPS analysis also indicated the loss if Mo and N after anodic activation (Fig. S26). The Ni ions were mostly in the +2 and +3 oxidation states (Fig. S26a), while the Fe ions were in the +3 oxidation state (Fig. S26c).The post-catalytic analysis indicated that the three catalysts were all mostly composed of iron nickel oxyhydroxides, whose structure should be simialr to that of the analogous Fe-NiO_x-NF.[23]

We probed the origin of the difference of activity between Fe-NiMo-NH_3/H_2 and Fe-NiO_x-NF. Both catalysts have similar high-resolution XPS spectra (Fig. S26 and S27). The SEM image

of Fe-NiMo-NH_3/H_2 revealed distinct hierarchical structure (Fig. S28a). In contrast, the Fe-NiO_x-NF electrode has a flat structure with wrinkled nanosheets (Fig. S28 b). Similar features were observed by TEM images (Figure 3a and Fig. S28c). Thus, Fe-NiMo-NH_3/H_2 has a rougher morphology than Fe-NiO_x-NF, which should provide more catalytic active sites and is more beneficial for electrolyte penetration and bubble escape. Consistent with this result, Fe-NiMo-NH_3/H_2 has up to 6.6 times higher ECSA than Fe-NiO_x-NF (Fig. S28d). Thus, the superior activity of Fe-NiMo-NH_3/H_2 is probably related to a favorable morphology and/or distribution of active sites due to its particular synthetic procedure. The initially foreseen effect of Mo and N is absent due to the loss of Mo and N during OER.

The geometric activity of NiMo-NH_3/H_2 in HER in alkaline medium is among the best among non-noble catalysts (Table S4). Likewise, the geometric activity of Fe-NiMo-NH_3/H_2 for in OER competes favourably among other catalysts (Table S5). The two catalysts can be easily prepared from a common $NiMoO_4$ precursor. As such, they are well suited for AEM electrolyser applications. Until now, only a few OER catalysts[10,12,26,27]such as $Cu_{0.7}Co_{2.3}O_4$, NiFe-LDH, $NiFe_2O_4$, $CuCoO_3$ and Co_3O_4, and a few HER catalysts[11,26,27]such as NiFeCo, Ni, and Ni/(CeO_2-La_2O_3)/C have been applied in AEM electrolyzers (Table S6). The performance of such systems remains modest. Motivated by these considerations, we tested NiMo-NH_3/H_2 and Fe-NiMo-NH_3/H_2 for AEM electrolysis.

The tests were conducted using membrane electrode assemblies (MEAs). We deposited the cathode and anode catalysts on carbon paper electrodes, which were separated by a sustainion anion exchange membrane (X37-50 grade T, Dioxide Materials) (Fig. S29). The electrolyser was then tested in a flowing 1 M KOH solution at different temperatures. The current-voltage behaviour of MEAs incorporating different NiMo-based catalysts is shown in Fig. 4a. In line with their catalytic activity, the efficiency of electrolysers follow the order of Fe-NiMo-

NH_3/H_2||NiMo-NH_3/H_2 > Fe-NiMo-NH_3||NiMo-NH_3 > Fe-NiMo-H_2/N_2||NiMo-H_2/N_2 > Fe-$NiMoO_4$||Fe-$NiMoO_4$ (Fig. 4a). The best MEA, with a Fe-NiMo-NH_3/H_2||NiMo-NH_3/H_2 cathode/anode configuration, delivered up to 1 A cm^{-2} at the cell voltage of 1.77 V at 20 °C (Fig. 4a). The stability of the Fe-NiMo-NH_3/H_2||NiMo-NH_3/H_2 MEA was confirmed in 25 h electrolysis tests at 50 and 500 mA cm^{-2}, where the cell voltages remained largely unchanged (Fig. 4b). The MEAs incorporating the three best NiMo-catalysts were further tested in 1 M KOH at different temperatures ranging from 20 °C to 80 °C (Fig. 4c). Increasing temperature led to lower cell voltages, but the performance trends were the same at all temperatures (Fig. S30). The best MEA incorporating Fe-NiMo-NH_3/H_2||NiMo-NH_3/H_2 catalysts had a cell voltage of only 1.52 V for 500 mA cm^{-2} at 80 °C (Fig. 4d). The energy conversion efficiencies (EF) of this MEA were then tested at 1 A cm^{-2} at different temperatures. The efficiencies increased from 69.7% at 20 °C to 75.1% at 80 °C (Fig. 4e). The best performance of non-noble metal catalysts for AEM electrolysis had been 1.9 V at 1 A cm^{-2} and 63.1% at 60 °C. For AEMs with noble metal (Pt/C) as catalysts, the best performance was the cell voltage of 1.59 V at 1 A cm^{-2}, corresponding to an efficiency of 74.3% at 80 °C (Fig. 4f and Table S6). Our AEM, with a cell voltage of 1.57 V at 1 A cm^{-2}, corresponding to an efficiency of 75.1% at 80 °C, outperforms all previous examples.

In summary, we developed superior HER and OER catalysts from on a same precursor, $NiMoO_4$. Annealing of $NiMoO_4$ in an atmosphere of NH_3/H_2, NH_3, H_2/N_2 at an elevated temperature resulted in three catalysts NiMo-NH_3/H_2, NiMo-NH_3, and NiMo-N_2/H_2, which all contained NiMo nanoparticles. The NiMo-NH_3/H_2 had the best HER activity thanks to an additional $NiMoN_x$ component. This catalyst delivered 500 mA cm^{-2} at an overpotential of only 107 mV, ranking it among the best HER catalysts for high current dentsities in alkaline medium. Anodic oxidation of the three NiMo-based catalysts in Fe-containing KOH resulted in three OER catalysts Fe-NiMo-NH_3/H_2, Fe-NiMo-N_2/H_2, Fe-NiMo-NH_3. These catalysts have a similar composition of FeNi oxyhydroxides but exhibit substanitally different activity. The

most active catalyst, Fe-NiMo-NH_3/H_2 , delivered 500 mA cm^{-2} at an overpotential of only 244 mV in OER, representing one of the most active OER catalysts at high current densities. The Fe-NiMo-NH_3/H_2 catalyst had high intrinsic activity as well, with TOFs about 10 times higher than a previous benchmark FeNi catalyst. The NiMo-NH_3/H_2 and Fe-NiMo-NH_3/H_2 had been applied as cathode and anode catalysts in an AEM electrolyzer, respectively. This electrolyzer delivered 1.0 A cm^{-2} at a cell voltage of only 1.57 V at 80 °C, with an energy conversion efficiency of 75.1%. This efficiency is the highest among all AEM electrolyzers, including those employing noble-metal catalysts. This work demonstrates the potential of earth-abundant electrocatalysts in water splitting devices, and provides a benchmark for AEM electrolyzers.

Supporting Information

Supporting Information is available from the Wiley Online Library or from the author.

Acknowledgements

This work is supported by the European Research Council (no. 681292). We thank Jun Gu (EPFL) for help with MEA tests.

Received: ((will be filled in by the editorial staff))

Revised: ((will be filled in by the editorial staff))

Published online: ((will be filled in by the editorial staff))

References

[1] J. Kibsgaard, I. Chorkendorff, *Nat. Energy* **2019**, *4*, 430–433.

[2] J. R. Varcoe, P. Atanassov, D. R. Dekel, A. M. Herring, M. A. Hickner, P. A. Kohl, A. R. Kucernak, W. E. Mustain, K. Nijmeijer, K. Scott, et al., *Energy Environ. Sci.* **2014**, *7*, 3135–3191.

[3] A. Marshall, B. Børresen, G. Hagen, M. Tsypkin, R. Tunold, *Energy* **2007**, *32*, 431–436.

[4] M. Carmo, D. L. Fritz, J. Mergel, D. Stolten, *Int. J. Hydrogen Energy* **2013**, *38*, 4901–4934.

[5] G. Schiller, R. Henne, P. Mohr, V. Peinecke, *Int. J. Hydrogen Energy* **1998**, *23*, 761–765.

[6] K. Zeng, D. Zhang, *Prog. Energy Combust. Sci.* **2010**, *36*, 307–326.

[7] C. C. Pavel, F. Cecconi, C. Emiliani, S. Santiccioli, A. Scaffidi, S. Catanorchi, M. Comotti, *Angew. Chemie Int. Ed.* **2014**, *53*, 1378–1381.

[8] X. Wu, K. Scott, *J. Mater. Chem.* **2011**, *21*, 12344–12351.

[9] S. H. Ahn, B.-S. Lee, I. Choi, S. J. Yoo, H.-J. Kim, E. Cho, D. Henkensmeier, S. W. Nam, S.-K. Kim, J. H. Jang, *Appl. Catal. B Environ.* **2014**, *154–155*, 197–205.

[10] W.-S. Choi, M. J. Jang, Y. S. Park, K. H. Lee, J. Y. Lee, M.-H. Seo, S. M. Choi, *ACS Appl. Mater. Interfaces* **2018**, *10*, 38663–38668.

[11] J. J. Kaczur, H. Yang, Z. Liu, S. D. Sajjad, R. I. Masel, *Front. Chem.* **2018**, *6*, 263.

[12] H. Koshikawa, H. Murase, T. Hayashi, K. Nakajima, H. Mashiko, S. Shiraishi, Y. Tsuji, *ACS Catal.* **2020**, *10*, 1886–1893.

[13] J. Zhang, T. Wang, P. Liu, Z. Liao, S. Liu, X. Zhuang, M. Chen, E. Zschech, X. Feng, *Nat. Commun.* **2017**, *8*, 15437.

[14] Y. Zhou, M. Luo, W. Zhang, Z. Zhang, X. Meng, X. Shen, H. Liu, M. Zhou, X. Zeng, *ACS Appl. Mater. Interfaces* **2019**, *11*, 21998–22004.

[15] A. Nairan, P. Zou, C. Liang, J. Liu, D. Wu, P. Liu, C. Yang, *Adv. Funct. Mater.* **2019**, *29*, 1903747.

[16] Y. An, X. Long, M. Ma, J. Hu, H. Lin, D. Zhou, Z. Xing, B. Huang, S. Yang, *Adv. Energy Mater.* **2019**, *9*, 1901454.

[17] W.-F. Chen, K. Sasaki, C. Ma, A. I. Frenkel, N. Marinkovic, J. T. Muckerman, Y. Zhu, R. R. Adzic, *Angew. Chemie Int. Ed.* **2012**, *51*, 6131–6135.

[18] T. Kou, S. Wang, J. L. Hauser, M. Chen, S. R. J. Oliver, Y. Ye, J. Guo, Y. Li, *ACS Energy Lett.* **2019**, *4*, 622–628.

[19] M. P. Suryawanshi, U. V Ghorpade, S. W. Shin, U. P. Suryawanshi, E. Jo, J. H. Kim, *ACS Catal.* **2019**, *9*, 5025–5034.

[20] B. Zhang, K. Jiang, H. Wang, S. Hu, *Nano Lett.* **2019**, *19*, 530–537.

[21] F. Song, X. Hu, *Nat. Commun.* **2014**, *5*, 4477.

[22] G. Chen, Y. Zhu, H. M. Chen, Z. Hu, S.-F. Hung, N. Ma, J. Dai, H.-J. Lin, C.-T. Chen, W. Zhou, et al., *Adv. Mater.* **2019**, *31*, 1900883.

[23] F. Song, M. M. Busch, B. Lassalle-Kaiser, C.-S. Hsu, E. Petkucheva, M. Bensimon, H. M. Chen, C. Corminboeuf, X. Hu, *ACS Cent. Sci.* **2019**, *5*, 558–568.

[24] Y. Pi, Q. Shao, P. Wang, F. Lv, S. Guo, J. Guo, X. Huang, *Angew. Chemie Int. Ed.* **2017**, *56*, 4502–4506.

[25] B. Zhang, X. Zheng, O. Voznyy, R. Comin, M. Bajdich, M. García-Melchor, L. Han, J. Xu, M. Liu, L. Zheng, et al., *Science.* **2016**, *352*, 333– 337.

[26] Y. Leng, G. Chen, A. J. Mendoza, T. B. Tighe, M. A. Hickner, C.-Y. Wang, *J. Am. Chem. Soc.* **2012**, *134*, 9054–9057.

[27] X. Su, L. Gao, L. Hu, N. A. Qaisrani, X. Yan, W. Zhang, X. Jiang, X. Ruan, G. He, *J.*

Memb. Sci. **2019**, *581*, 283–292.

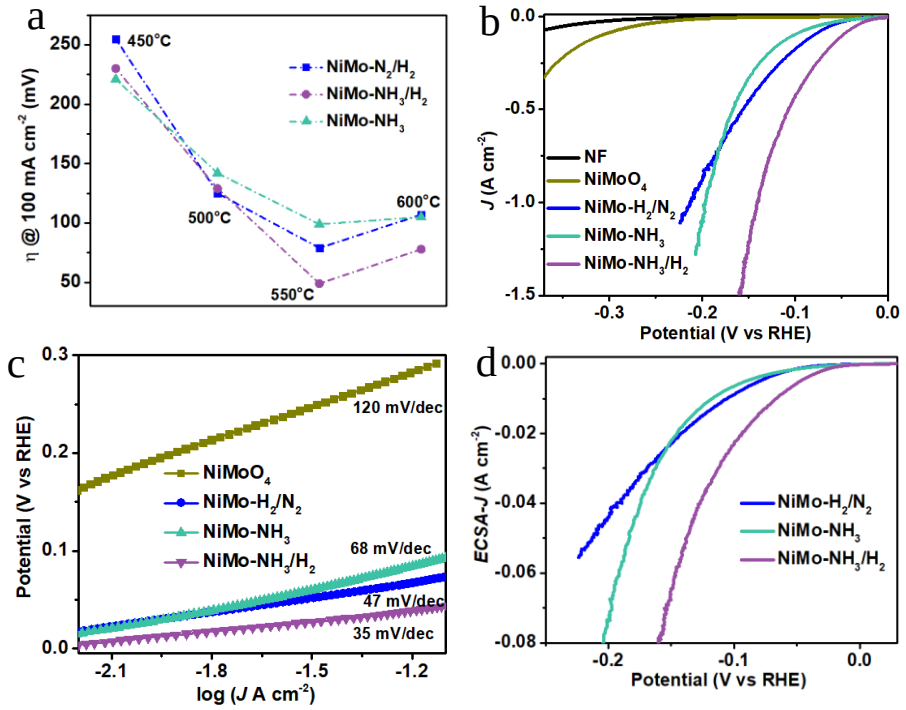

Figure 1 a) HER activity of NiMo catalysts against annealing temperature; b) Polarization curves and c) corresponding Tafel slopes of NiMo-NH_3/H_2, NiMo-NH_3, NiMo-N_2/H_2, $NiMoO_4$ and NF for HER in 1 M KOH. Loading of catalysts on NF are about 2.0, 2.0, 1.9, 2.5 mg cm^{-2}, respectively. IR-corrected, Scan rate: 1mv/s. d) Comparison of ECSA-normalized activity of different catalysts.

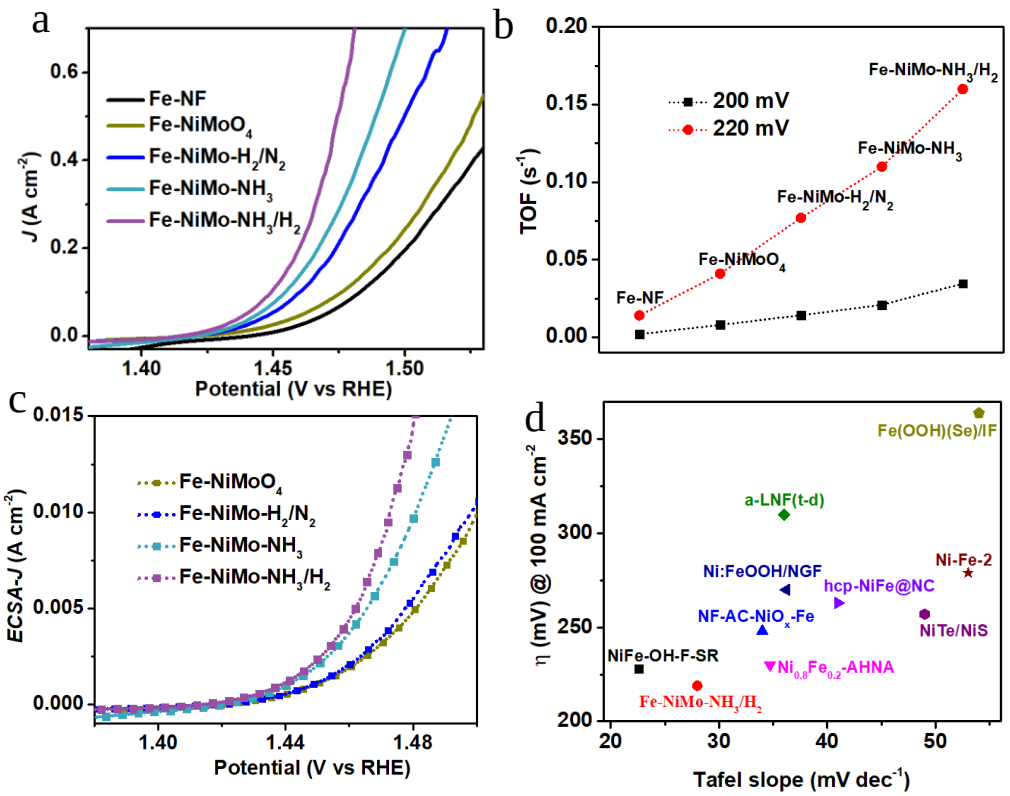

Figure 2 a) Polarization curves of Fe-NiMo-NH_3/H_2, Fe-NiMo-N_2/H_2, Fe-NiMo-NH_3, Fe-$NiMoO_4$ and Fe-NF for OER in 1 M KOH. Backward scan; IR-corrected, Scan rate: 1mV/s. b) The TOFs of different catalysts at the overpotentials of 200 and 220 mV. c) The ECSA-normalized activity of different catalysts. d) Comparison of Tafel slopes and overpotential for 100 mA cm^{-2} for state-of-the-art catalysts containing Ni and/or Fe.

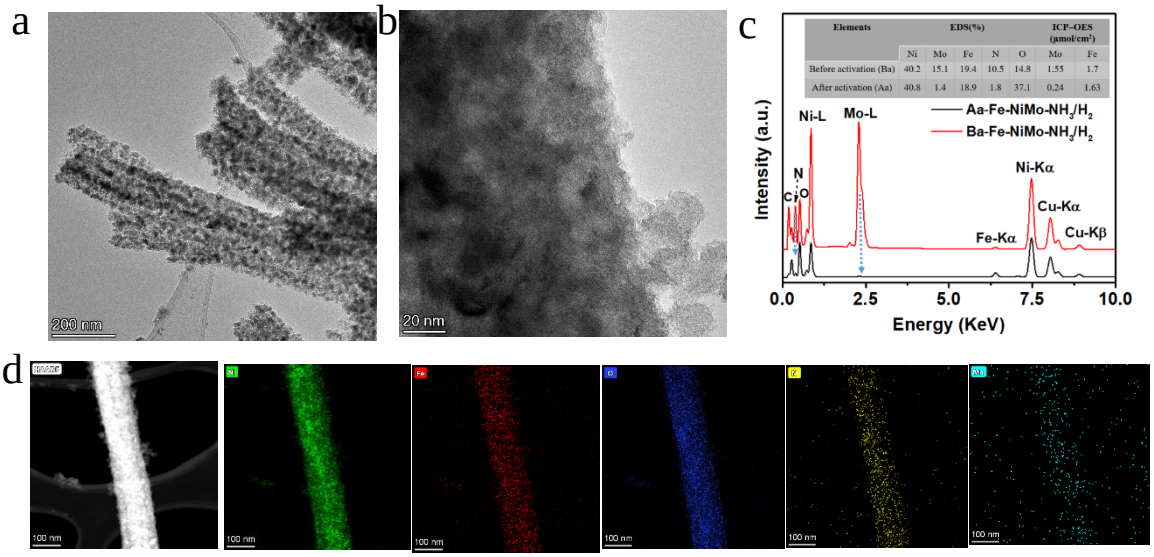

Figure 3 a) TEM image and b) HRTEM image of the Fe-NiMo-NH_3/H_2 catalyst after anodic activation. c) The EDS spectrum and corresponding element contents (EDS and ICP-OES) of Fe-NiMo-NH_3/H_2 catalyst before and after anodic activation. (d) Elemental mapping images of Fe-NiMo-NH_3/H_2 catalyst after anodic activation.

Table 1. Comparison of OER performance of Fe modified NiMo catalysts.

Catalysts	OER performance							Loading mass
	$\eta_{100\ mA/cm^2}$ (mV)	$\eta_{500\ mA/cm^2}$ (mV)	TOF_{220mV} (s^{-1})	Tafel slope (mV dec^{-1})	C_{dl} (mF cm^{-2})	ECSA	R_{ct} (Ω)	FeOOH (ug cm^{-2})
Fe-NiMo-NH_3/H_2	219	244	0.16	28	3.7	45.7	7.3	151
Fe-NiMo-N_2/H_2	230	270	0.077	28	3.9	48.1	9.7	160
Fe-NiMo-NH_3	224	259	0.11	29	3.0	37.0	8.6	155
Fe-$NiMoO_4$	245	296	0.041	34	2.0	24.7	28.4	142
Fe-NF	251	307	0.014	/	/	/	/	138

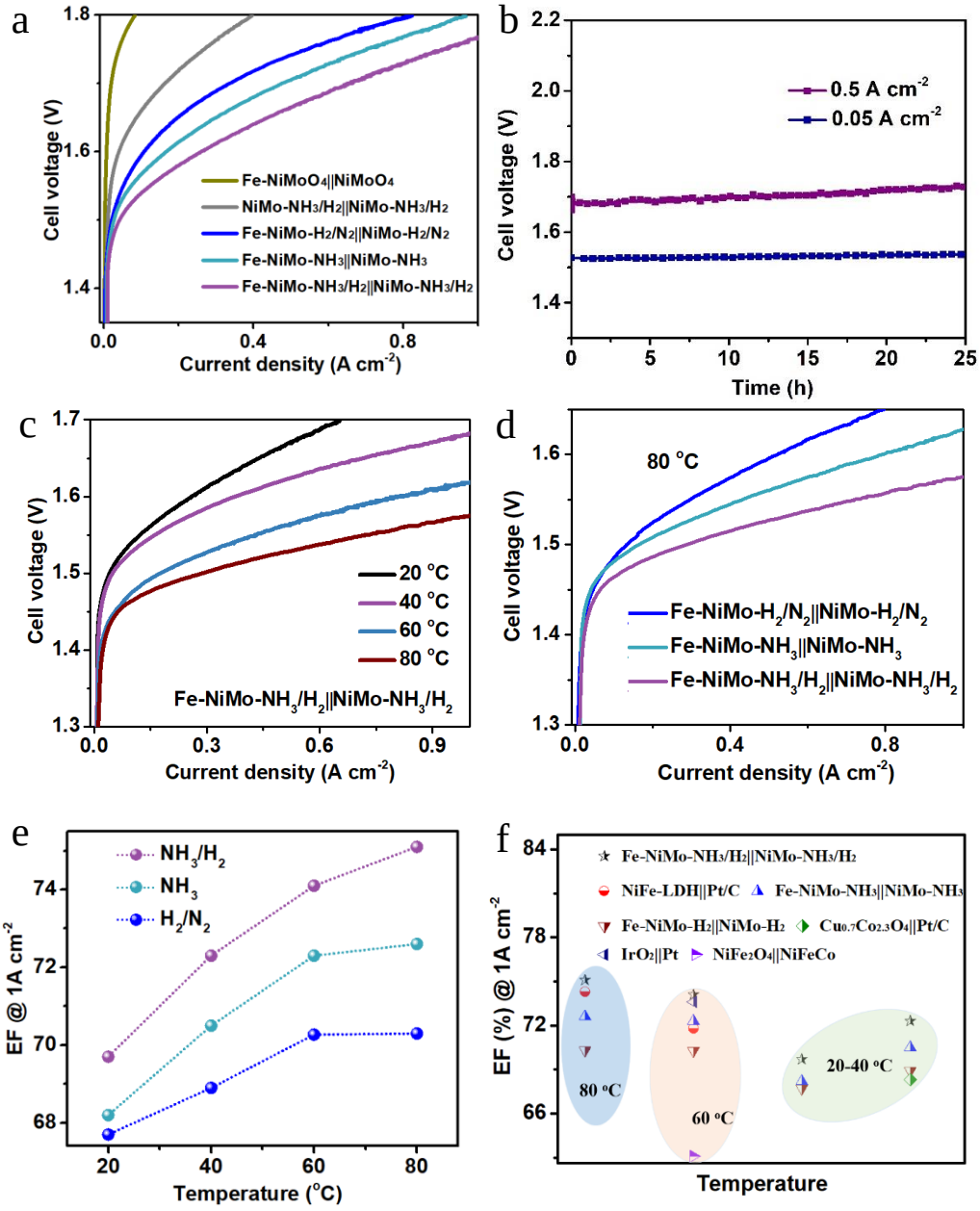

Figure 4 a) The performance of MEAs employing a series of cathode/anode catalysts. b) Durability of the MEAs using the Fe-NiMo-NH_3/H_2||NiMo-NH_3/H_2 as catalyst at the current density of 0.05 and 0.5 A cm^{-2}. c) The performance of MEAs employing Fe-NiMo-NH_3/H_2||NiMo-NH_3/H_2 as catalyst at different temperatures. d) The performance of MEAs employing Fe-NiMo-NH_3/H_2||NiMo-NH_3/H_2, Fe-NiMo-NH_3||NiMo-NH_3, Fe-NiMo-N_2/H_2||NiMo-N_2/H_2 pairs at 80 °C. e) The energy efficiencies of MEAs employing different catalysts from 20 °C to 80 °C. f) Comparison of efficiencies of the MEAs for Fe-NiMo-NH_3/H_2||NiMo-NH_3/H_2 pair with state-of-the-art examples.

Table of Contents Graphic

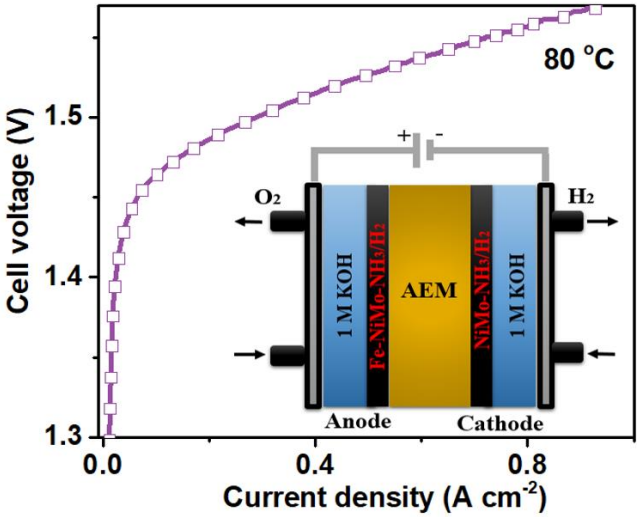

Superior HER and OER catalysts have been developed by chemical processing a common NiMo oxide. An AEM electrolyzer employing these electrocatalysts deliveres an energy conversion efficiency of 75.1% at 80 °C, providing a benchmark for alkaline AEM electrolyzers.